Controlling micro- and nanofibrillar morphology of polymer blends in low-speed melt spinning process. Part I. Profiles of PLA/PVA-filament parameters along the spinline

Nguyen Hoai An Tran,[1,2] **Harald Brünig,**[1] **Gert Heinrich**[1,3]

[1]Leibniz-Institut für Polymerforschung Dresden e. V, Hohe Straße 6, Dresden 01069, Germany
[2]Ho Chi Minh City University of Technology, VNU–HCM, Ho Chi Minh City, Viet Nam
[3]Institut für Werkstoffwissenschaft, Technische Universität Dresden, Dresden 01062, Germany
Correspondence to: N. H. A. Tran (E-mail: tnhoaian@gmail.com) and H. Brünig (E-mail: bruenig@ipfdd.de)

ABSTRACT: The profiles of PLA/PVA filament parameters (e.g., temperature, velocity, tensile stress, and apparent elongational viscosity) along the spinline in the low-speed melt spinning process under various spinning conditions were investigated. Owing to the combination of the filament velocity and filament temperature measurements using laser doppler velocimetry (LDV) and infrared thermography, respectively, the fiber formation zone was determined. The length of the fiber formation zone obtained from filament velocity profiles L_{Sv} is always shorter than that obtained from the filament temperature profiles L_{ST} ($L_{Sv} < L_{ST}$). Obviously, this unexpected phenomenon occurs for low spinning speeds due to the axial heat conduction effect of the filament along the spinline and the nonuniform radial temperature distribution through the cross-sectional thick filament. Another remarkable finding is related to the Nusselt number which has been found as nearly constant along the spinline in the low-speed melt spinning process. Thus, mathematical simulations of the filament temperature profiles will be simplified drastically. © 2016 Wiley Periodicals, Inc. J. Appl. Polym. Sci. **2016**, *133*, 44258.

INTRODUCTION

The melt spinning process of polymer blends resulting into micro-/nanofibers has been known since 1960s and the first patent of the fibrillation of polymer blends in elongational flow was issued to Miller and Merriam in 1963.[1] Polymeric micro-/nanofibers obtained by melt extrusion and melt spinning of polymer blends with further extraction of the matrix polymer have become again the subject of intensive investigations over the last 5 to 10 years due to a tremendous increase for economic and environmental concerns.[2–5] Recently, a novel and simple fabrication process for producing biodegradable and biocompatible nanofibrillar poly(lactic acid) structures from poly(lactic acid) (PLA) and poly(vinyl alcohol) (PVA) blends has been successfully developed by using the conventional melt spinning method of polymeric fibers on the industrial-scale melt spinning device with twin-screw extruder.[6] Thus, for the first time, different PLA/PVA filaments with different finenesses were fabricated. The produced PLA fibrils after removing the PVA matrix from PLA/PVA filaments were in nanometer range with an average diameter varying from 44 to 85 nm depending on take-up velocities and draw ratios. The PLA

scaffolds made from PLA/PVA filaments could be promising candidates as scaffolds for tissue engineering due to their outstanding biocompatibility and a large-surface-area-to-volume ratio.

Our recent study[7] focused on the understanding of the morphology development of PLA/PVA blend and the mechanism of the fibrillation process within fiber formation zone. It was found that during melt spinning, the rod-like structures of the dispersed PLA phase in PLA/PVA blend are stretched and coalesced to form continuous long thin nanofibrils. Although this study[7] has been limited for the special spinning condition with the take-up velocity of 50 m min^{-1} and the mass flow rate of 1.0 g min^{-1}, it confirms that melt spinning is an effective method to form the dispersed phase into continuous fibrillar structures due to the presence of an elongational flow. The increase of the velocity and tensile stress in the fiber formation zone are mainly responsible for the stretching and coalescence of the dispersed PLA phase into nanofibrils in the PVA matrix of polymer blends.

However, there are still many questions to explore: can the short rod-like structures of the dispersed PLA phase always form the

long thin fibrils with different flow rates and/or take-up velocity? Are the sizes (lengths and diameters) of the final PLA nanofibrils caused by only the deformation of their initial sizes at die exit or by the combination of the deformation, coalescence, and break-up processes? Can the changes in spinning conditions control the deformation, coalescence, and break-up processes of the dispersed PLA phase in PLA/PVA filaments within fiber formation zone?

To answer these questions, our current research activities simultaneously focus on both the study of morphological development of PLA/PVA blends at different location along the spinline under different spinning conditions and on the characterization of profiles of all filament parameters such as filament temperature, velocity, diameter, tensile force, tensile stress, and apparent elongational viscosity. It is well known that during melt spinning, the morphology development of polymer blends along the spinline is caused by the changes of these filament parameters.

This article, as a first part in a three-part series of our current studies, presents the results regarding the characterization of PLA/PVA filament parameter profiles along the spinline in the low-speed melt spinning process under different spinning conditions. Special attention of the characterization activity of the filament parameter profiles was given on the determination of the fiber formation zone, where the fibrillation process of the dispersed PLA phase mainly occurred. In this study, the length of fiber formation zone was determined from both filament velocity and filament temperature profiles. The filament velocity profiles were obtained by measuring the filament velocity using the laser doppler velocimetry (LDV). The filament temperature along the spinline was investigated using the infrared thermography. Based on these experimental results of filament temperature, the Nusselt number, which describes the heat transfer from filament surface into the surrounding air, was determined. The Nusselt number is found to be nearly constant along the spinline in the low-speed melt spinning process. This drastically simplifies mathematical simulations of the filament temperature profile along the spinline.

THEORETICAL CONSIDERATIONS OF THIN-FILAMENT-MODEL

Mathematical models of the dynamic of the fiber formation in the melt spinning process are often described by using the thin-filament model with assumptions: uniform distribution of axial velocity and temperature across the filament. In other words, radial distribution of axial velocity and temperature are neglected.[8] The thin-filament model is based on the following simplifying assumptions: (i) vertical spinline, and (ii) the steady and incompressible melt flow.

The following subsections review briefly the basic balance equations of the thin-filament model of the melt spinning process that describe deformation, cooling, and stress development processes of filaments. More complete and accurate details of mathematical modeling were discussed and reviewed in four monographs by Ziabicki in 1976,[9] Ziabicki and Kawai in 1985,[10] Nakajima et al. in 1994,[11] and by Beyreuther and Brünig in 2007.[12]

Mass Balance Equation

The mass balance is described by the continuity equation of the melt spinning process:

$$Q = \varrho_P(x) \cdot A(x) \cdot v(x) = \text{ constant or} \tag{1}$$

$$Q = \varrho_P(x) \cdot \frac{\pi}{4} D(x)^2 \cdot v(x) \tag{2}$$

where Q is the mass flow rate, $\varrho_P(x)$, $v(x)$, $D(x)$, and $A(x)$ denote, respectively, the mass density of polymer, the filament velocity, the circular cross-sectional diameter, and the cross-sectional area of filament at a distance x from the spinneret.

Force Balance Equation

The force balance equation can be used to determine the forces acting on the filament and was introduced for the first time by Ziabicki.[13] The force contributions are given as follows[11]:

$$F(x) = F_L - F_{\text{grav}}(x) + F_{\text{surf}}(x) + F_{\text{aero}}(x) + F_{\text{inert}}(x) \tag{3}$$

where F_L is the take-up force, applied to the filament by the take-up device, $F_{\text{surf}}(x)$ is the surface tension force, $F_{\text{grav}}(x)$ is the gravitational force, $F_{\text{aero}}(x)$ is the air drag force, and $F_{\text{inert}}(x)$ is the inertial force. These forces at any distance x from the spinneret can be expressed as follows:

$$F_{\text{grav}}(x) = \int_x^L \varrho_P \cdot g \cdot \dot{V}/v(\tilde{x}) \, d\tilde{x} \tag{4}$$

$$F_{\text{surf}}(x) = \pi \cdot \sigma_{\text{surf}} \cdot (R_0 - R(x)) \tag{5}$$

$$F_{\text{aero}}(x) = 2\pi \int_0^x R(\tilde{x}) \cdot \frac{\varrho_{\text{air}}}{2} \cdot v^2(\tilde{x}) \cdot c_f(\tilde{x}) \cdot d\tilde{x} \tag{6}$$

$$F_{\text{inert}}(x) = Q \cdot (v(x) - v_0) \tag{7}$$

where, $\dot{V}$ is the volumetric flow rate, v is the velocity of filament, σ_{surf} is the surface tension of the material, R_0 is the initial radius of filament, ϱ_{air} is the mass density of air, and c_f is the friction coefficient of air. The air friction coefficient c_f describes the friction-caused momentum transfer between filament surface and ambient air. The air friction coefficient c_f depends on the state of air flow surrounding the filament within fiber formation zone. Experimental investigations on air friction forces acting on the running filament by Hamana[14] led to the often used following equation:

$$c_f = 0.37 \cdot \text{Re}^{-0.61} \tag{8}$$

where Re denotes the dimensionless Reynolds number. The Reynolds number itself is given by

$$\text{Re}(x) = \frac{\varrho_{\text{air}} \cdot v(x) \cdot D(x)}{\eta_{\text{air}}} \tag{9}$$

where η_{air} is the dynamic viscosity of air.

Energy Balance Equation

Based on the energy balance equation,[9] the change of the filament temperature is given by

$$\frac{dT(x)}{dx} = -(T(x) - T_{\text{air}}(x)) \cdot N_u \frac{\pi \cdot \lambda_{\text{air}}}{Q \cdot c_P} + \frac{\Delta H}{c_P} \cdot \frac{dX_c}{dx} \tag{10}$$

where $T_{\text{air}}(x)$ is the temperature of surrounding air, λ_{air} is the heat conductivity of air, $Q = \varrho_P \cdot \dot{V}$ is the mass flow rate of polymer in which ϱ_P is the mass density of the polymer blend, and $\dot{V}$ is the volumetric flow rate, c_P represents the specific heat

Table I. Melting- and Glass Transition Temperatures of PLA, PVA, and PLA/PVA 30/70 Blend

	PLA	PVA	PLA/PVA 30/70
Melting temperature (°C)	160	174	160 and 176
Glass transition temperature (°C)	61	34	55 and 41

capacity of the polymer, ΔH is the heat of fusion and X_c is the crystallinity degree, and N_u is the Nusselt number, characterizing the heat transfer from filament surface into the surrounding air. The Nusselt number N_u for air flowing parallel to a cylinder is often calculated using the following common equation that was developed by Kase and Matsuo[15]:

$$N_u = 0.42 \cdot Re_\parallel^{0.334} \qquad (11)$$

where $Re_\parallel$ is the Reynolds number related to the parallel air flow that can be calculated using the above eq. (9).

EXPERIMENTAL

Materials and Blend Preparations

The PLA 6202D (purchased from NatureWorks LLC) and the PVA (Mowiflex TC 232, kindly donated by Kuraray Co., Ltd, Japan) were used for the melt spinning of PLA/PVA blends. Table I summarizes the melting temperatures and glass transition temperatures of the PLA, PVA, and PLA/PVA 30/70 blends obtained using different scanning calorimetry (DSC).

The PLA/PVA blend pellets at weight ratio of 30/70 were melt compounded using a HAAKE Poly Lab OS twin screw extruder (PTW 16/25, Thermo Fisher Scientific Germany BV & Co KG, Braunschweig, Germany). The mixing temperatures at different zones along the extruder (starting from the feeding zone to the die) were 175 °C, 180 °C, 185 °C, 190 °C, 190 °C, and 180 °C. The screw speed was 100 rpm with the feeding rate of 1000 g/h. The mixed extrudates were then cut into small pellets. These pellets were melt spun as PLA/PVA-monofilament on a piston spinning device.

Melt Spinning

The melt spinning experiments were carried out using a self-constructed piston type spinning device at the Leibniz-Institut für Polymerforschung Dresden e. V. (IPF Dresden). The schematic drawing and the principle of this device were found in Ref. 7 with the following specifications: The diameter and the length of the capillary hole was $D_0 = 0.6$ mm and $L = 1.2$ mm, respectively.

The spinning conditions for spinning processes are shown in Table II; for instance, the take-up velocity is altered from 10 m min^{-1} to 70 m min^{-1} at a constant flow rate of 1 g min^{-1} (condition B) and the flow rate is also varied at a constant take-up velocity of 50 m min^{-1} (condition A). Before melt spinning, the PLA/PVA pelletized blends were dried in a vacuum oven at a temperature of 60 °C for 6 h and then filled into the cylinder under dry nitrogen. All spinning experiments were performed at 195 °C.

Online Filament Temperature Measurements

The filament temperature was measured using an infrared camera VarioTHERM^{TM} with microscope lens MWIR/f4.4, designed by Jenoptik AG, Jena, Germany, combined with the monitoring subsystem including a personal computer (PC) and software package IRBIS$^{®}$ supported by InfraTec GmbH, Dresden, Germany. More details on this infrared thermography device are given by Golzar et al.[16]

The infrared thermography method for measuring the filament temperature is based on using infrared radiation. The radiated energy received by the infrared camera E includes three components: emitted E_e, reflected E_r, and transmitted energy E_t and can be expressed as follows:

$$E = E_e + E_r + E_t \quad \text{or} \qquad (12)$$

$$1 = \frac{E_e}{E} + \frac{E_r}{E} + \frac{E_t}{E} \qquad (13)$$

The eq. (13) can be simplified as follows:

$$1 = em + re + tr \qquad (14)$$

where em is the emissivity, which indicates the ability of infrared energy of filament emitted to infrared camera, the reflectivity re and the transmittivity tr indicating the ability to reflect and transmit infrared energy, respectively.

For a perfect black body, the emissivity em is equal one; the reflectivity re and the transmittivity tr are zero ($em = 1$, $re = 0$, and $tr = 0$). Polymeric filaments are not perfect black bodies and the emissivity of polymeric filaments is known less than 1 ($em < 1$) due to the optical and geometric properties (filament fineness) of the filament. Thus, it is necessary to find the relationship between the emissivity and the filament diameter in the case of the PLA/PVA filament.

In that regard, the two heated, fixed and polished drums with two different diameters 100 mm and 193 mm were employed. This method has been successfully utilized by our research group with following assumptions[16,17]: no or negligible small emissivity of the polished drums, the filament has the same temperature as the heated drum.

The spun PLA/PVA-monofilament was wrapped around the polished drums, which were electrically heated (Figure 1). The drum and the filament temperatures were determined using the infrared camera at different temperatures over the ranges from 50 °C to 200 °C and different filament diameters ranging from about 140 to 380 μm.

Figure 2 plots the emissivity of the thick PLA/PVA filaments versus their diameter in comparison with the emissivity of the fine polyetheretherketone (PEEK) filament.[16] It is seen that the emissivity of PLA/PVA filaments increases with the increasing of filament diameter and nearly reaches a constant value of about 0.8 with filament diameters more than 300 μm. The emissivity value of the present study for the thick PLA/PVA filaments is around 0.8. This value is much more that of the investigation by Golzar et al.,[16] when they studied the dependence of the emissivity of fine polyetheretherketone (PEEK) filament on its diameter. However, it is seen that the emissivity profiles versus diameter of both studies seem to be have a good relation and

Table II. Spinning Conditions with an Extrusion Temperature of 195 °C, $D_0 = 0.6$ mm, $L/D = 2$

Conditions	Take-up velocity (m min^{-1})	Volumetric flow rate (cm^3 min^{-1})	Mass flow rate (g min^{-1})
A	50	0.393	0.5
		0.785	1.0
		1.178	1.5
		1.570	2.0
B	10		
	30	0.785	1.0
	50		
	70		

have the similar increasing tendency with the increase of the filament diameter.

Online Filament Speed Measurements

Online measurements of the velocity were performed by using a laser doppler anemometry (LDA) device Laser Speed LS50M, manufactured by TSI Inc. It consists of optical sensor (model 250100), processor LS50MP, and a PC with configuration software TSI LaserTrak^{TM} (version 3.4) manufactured by TSI Inc. based on technique known as LDV. More details about this laser speed system are referred to Refs. 16 and 18. In the present study, velocity recordings were obtained at distances in the range of 2.5 to 50 cm from the die exit, at each 2.5 cm intervals. A set of 100 data points was gathered for each distance from the spinline.

Online Tension Measurement

Measurements of filament tension were carried out using a Tensiometer DIGITENS® 485 for hand-held measurement with the measuring head Type 125.120.1 by Honigmann Industrielle Elektronik GmbH. Before the measurement of the filament tension, the Tensiometer was set at zero and was calibrated using various metal plates of 2, 5, and 10 g, which attached to the PLA/PVA filament. During the filament was manually moved up and down through the measuring head, the full range of the Tensiometer was adjusted.

For the tension measurement of the running filament, the measuring head was located at 180 cm from the die exit just above the take-up device. Ten measurements were manually observed and an average value was calculated.

RESULTS AND DISCUSSION

Filament Temperature Profiles

Figure 3 shows the temperature profiles $T(x)$ of PLA/PVA filament along the spinline for the take-up velocity of 50 m min^{-1} with the mass flow rate of 1.0 g min^{-1} over the distances from 2.5 cm to 150 cm. The gray cross symbols ($\times$) represent the temperature values obtained using an infrared camera, the red points (●) (including deviation) are the corrected temperatures by the emissivity, which depend on the filament diameter as shown in Figure 2, and the red dash curve (— — —) is the fitted temperature profile using an exponential decay function. To have a better overview of the filament temperature profiles of seven different spinning conditions, only the fitted temperature profiles are presented in this section. More details of the experimental results, the fitted and simulated filament temperature profiles are completely described and discussed in Appendix.

It is seen that the filament temperature profiles substantially depend on the mass flow rates. The filament cooled more slowly along the spinline when the mass flow rate increased at the constant take-up velocity (Figure 4). In contrast, the filament temperature profiles seem to be independent of take-up velocities at the constant mass flow rate of 1.0 g min^{-1} and have the similar temperature profiles corresponding to the same following fitting eq. (15) (Figure 5):

$$T(x) = 25 + 170 \times \exp\left(-\frac{x}{42}\right) \tag{15}$$

where $T(x)$ is the filament temperature in °C at any distance x in cm from the die exit.

It is worth mentioning here that the glass transition temperature T_g of PLA/PVA filaments is assumed equal to T_g of PLA/PVA blend obtained using DSC measurement. From Table I, it is seen that the $T_{g,PLA} = 55$ °C is higher than the $T_{g,PVA} = 41$ °C in PLA/PVA 30/70 blend. Thus, the PLA solidifies first and the PLA/PVA blend is totally solidified at the glass transition temperature of PVA.
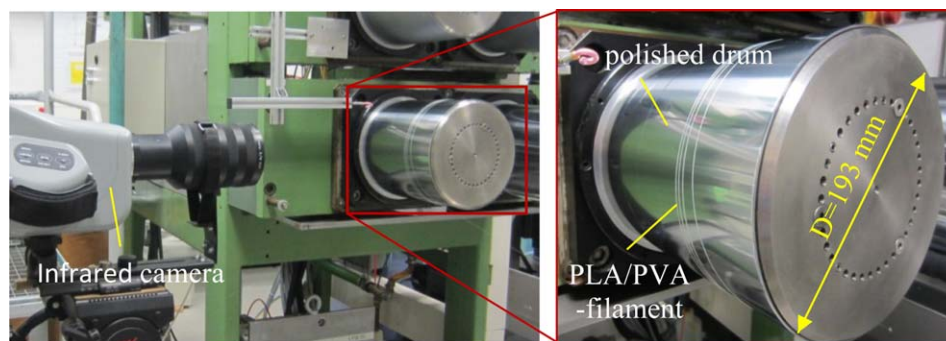

Figure 1. Photographic of test stand for measurement the emissivity as correction factor. [Color figure can be viewed in the online issue, which is available at wileyonlinelibrary.com.]
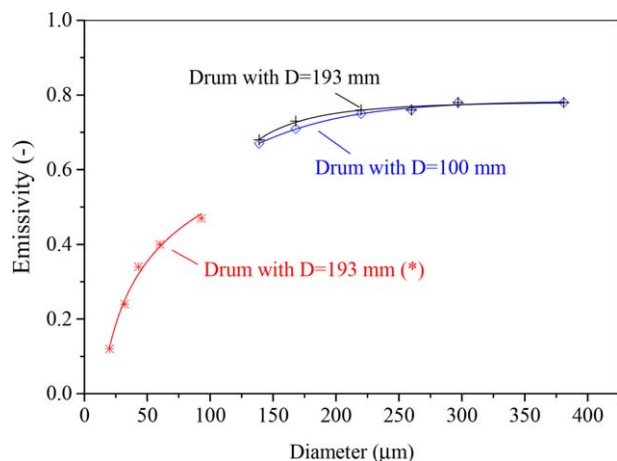
Figure 2. Emissivity vs. the diameter of PLA/PVA filaments in comparison with pure PEEK filament (*) adapted from Ref. 16. [Color figure can be viewed in the online issue, which is available at wileyonlinelibrary.com.]

Filament Velocity and Velocity Gradient along the Spinline

Figure 6 shows the velocity $v(x)$ profile of PLA/PVA blend monofilament along the spinline for the take-up speed of 50 m min^{-1} with the mass flow rate of 1.0 g min^{-1}. It should be noted that the gray cross symbols (×) represent for the velocity values obtained using a LDA device and the spinline-connected curve is the fitted curve by manual adjustment.

Figure 7(a) shows the manual fitted curves of the filament velocities versus distance to spinneret for the melt spinning processes with a constant take-up velocity of 50 m min^{-1} and mass flow rates over the range from 0.5 g min^{-1} to 2.0 g min^{-1}. Figure 7(b) represents the axial velocity gradient of the filament velocities versus distance to spinneret. The axial velocity gradient or the axial strain rate (ASR) is used to characterize the deformation behavior of the material. The ASR is determined by taking the derivative of $v(x)$ with respect to x: $v'(x) = dv(x)/dx$. Thus, the ASR is not constant along the spinline due to the increase of velocity. It has a maximum value at position in which the velocity changes largest amount per time. From the Figure 7(b), it is seen that the maximum value of the ASR decreases with increasing mass flow rate at the constant take-up velocity. At a higher flow rate, the ASR maximum region has a broader distribution and the ASR maximum peak slightly shifts towards longer distances from the spinneret.

Figure 8 shows the filament velocity and the ASR profiles along the spinline for the melt spinning processes with take-up velocities over the range from 10 m min^{-1} to 70 m min^{-1} at a constant mass flow rate of 1.0 g min^{-1}. It is seen from Figure 8(b) that the maximum value of the ASR increases with the increase of take-up velocity. The region of the ASR maximum value did not change much and is located at a distance of about 10 to 13 cm from the spinneret for various take-up velocities with the exception of the take-up velocity of 10 m min^{-1}, which its ASR profile shows a maximum value at a region of about 6 to 9 cm.

Filament Diameter Profiles

The filament diameter $D(x)$ along the spinline was calculated from velocity data $v(x)$ and volumetric flow rate $\dot{V}$ by the eq. (16) below:
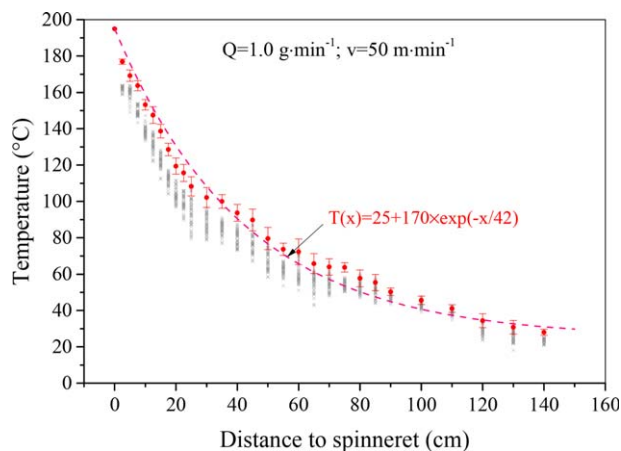

Figure 3. Filament temperature vs. distance for the take-up velocity of 50 m min^{-1} and the mass flow rate of 1 g min^{-1}: (×) uncorrected temperatures obtained using the infrared camera, (●) corrected temperatures, and (— — —) fitted temperature profile using an exponential decay function. [Color figure can be viewed in the online issue, which is available at wileyonlinelibrary.com.]

$$D(x) = \frac{2}{\sqrt{\pi}} \times \sqrt{\frac{\dot{V}}{v(x)}} \qquad (16)$$

where the filament velocity $v(x)$ at any distance x along the spinline was measured using the LDV.

It is seen that the change in mass flow rate has a substantial effect on the termination of filament attenuation process. The filament diameters of lower mass flow rates attenuate much more rapidly than that of higher mass flow rates and they reach their final diameters at a location closer to the die exit from [Figure 9(a)]. This is because that as the mass flow rate decreases, the filament reaches the solidification temperature faster (Figure 4). In contrast, the take-up velocities almost did not have an effect on the termination of filament attenuation
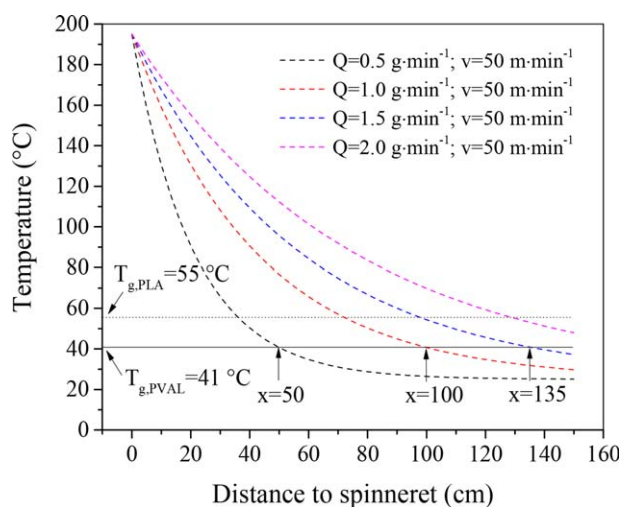

Figure 4. Filament temperature versus distance for the take-up velocity of 50 m min^{-1} and the different mass flow rates: 0.5, 1.0, 1.5, and 2.0 g min^{-1}. [Color figure can be viewed in the online issue, which is available at wileyonlinelibrary.com.]
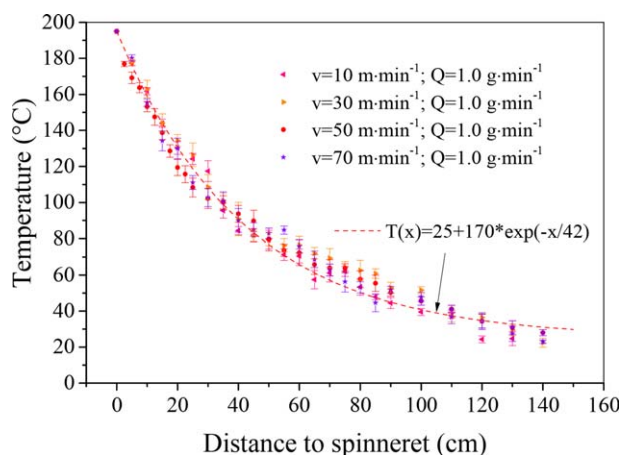
Figure 5. Filament temperature versus distance for the different take-up velocities at constant mass flow rate of 1.0 g min^{-1}. [Color figure can be viewed in the online issue, which is available at wileyonlinelibrary.com.]

process [Figure 9(b)]. The filament diameters reach their final value at the similar distance from the die exit, because the change of filament temperature along the spinline has the similar behavior (Figure 5).

Tensile Force, Stress, and Apparent Elongational Viscosity along the Spinline

In the melt spinning processes with low spinning speed up to about 750 m min^{-1}, the surface tension force $F_{surf}(x)$, the air drag force $F_{aero}(x)$ and the inertial force are usually negligible as small as compared to the take-up force F_L and the gravitational force $F_{grav}(x)$.[15,19–21] In this study, therefore, the tensile forces $F(x)$ are calculated using the momentum balance eq. (3) that can be simplified as follows:

$$F(x) \approx F_L + F_{grav}(x) \qquad (17)$$

where F_L is the take-up force. The gravitational force $F_{grav}(x)$, the weight of the filament at any distance x, can be calculated from the eq. (18):
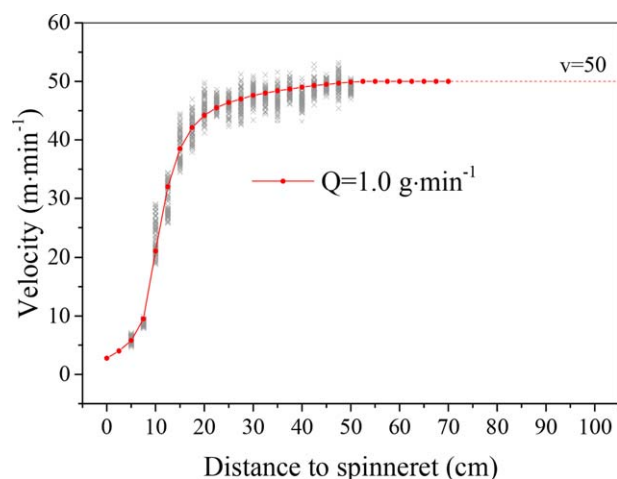
Figure 6. Velocity versus distance for the specific melt spinning condition: $v = 50$ m min^{-1}; $Q = 1$ g min^{-1}. [Color figure can be viewed in the online issue, which is available at wileyonlinelibrary.com.]

$$F_{grav}(x) = \int_x^L \varrho_P.g. \ \dot{V}/v(\tilde{x}).d\tilde{x} \qquad (18)$$

where g is the gravitational acceleration on earth ($g \approx 9.81$ m s^{-2}) and L is the take-up distance.

The tensile stress $\sigma(x)$ is given by the eq. (19)

$$\sigma(x) = F(x)/A(x) \qquad (19)$$

where $F(x)$ is the tensile force and $A(x) = \dot{V}/v(x)$ denotes the cross-sectional area of the filament.

Apparent elongational viscosity (APEV) $\eta_{app}(x)$ along the spinline was calculated by the following eq. (20):

$$\eta_{app}(x) = \sigma(x)/v'(x) \qquad (20)$$

where $\sigma(x)$ is the tensile stress and $v'(x)$ is the derivative of $v(x)$ with respect to x.

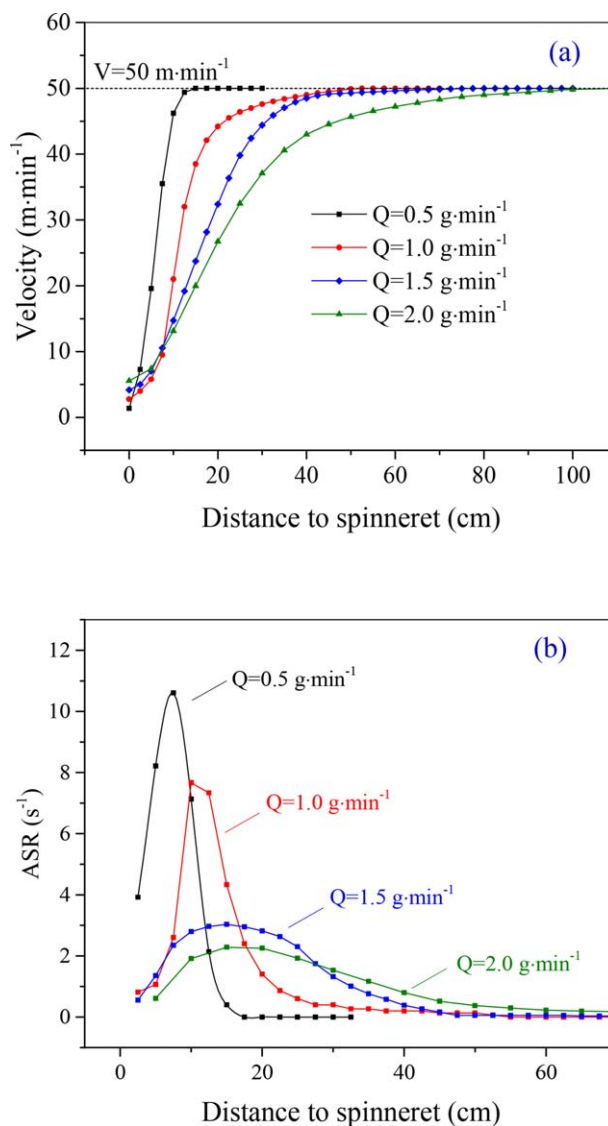**Figure 7.** Velocity (a) and axial strain rate (ASR) versus distance (b) for the melt spinning conditions: $v = 50$ m min^{-1}; $Q = 0.5$, 1.0, 1.5, and 2.0 g min^{-1}. [Color figure can be viewed in the online issue, which is available at wileyonlinelibrary.com.]
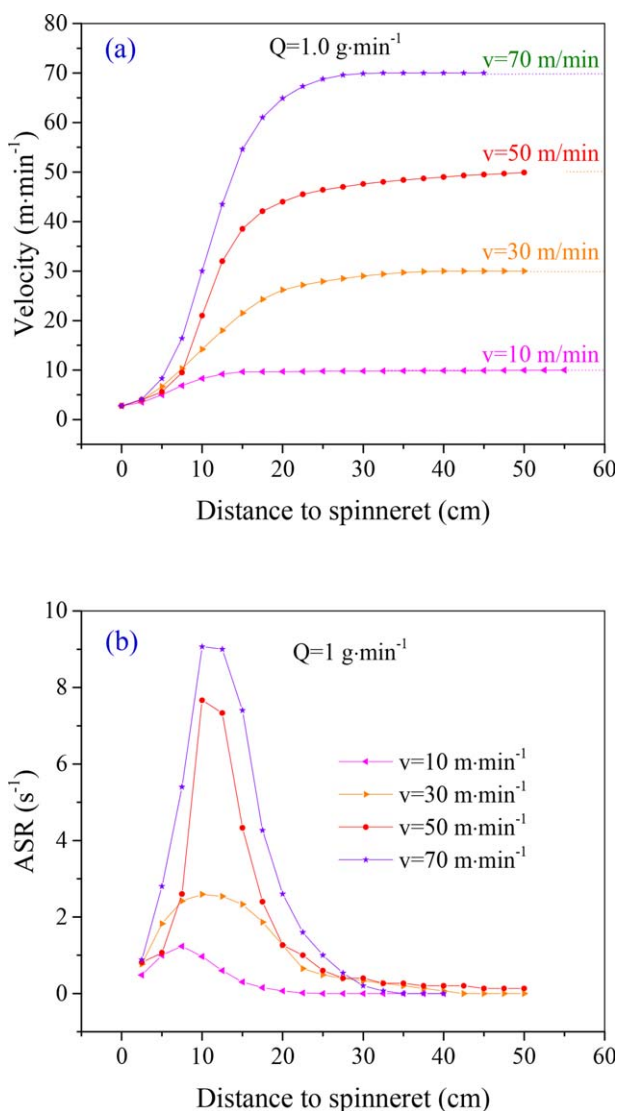
Figure 8. Velocity (a) and ASR (b) versus distance for the melt spinning conditions: $Q = 1.0$ g min^{-1}; $v = 10$, 30, 50, and 70 m min^{-1}. [Color figure can be viewed in the online issue, which is available at wileyonlinelibrary.com.]

In this study, the take-up force $F_L = 1.9$ cN was determined at a distance of 180 cm below the die exit and near take-up device using a Tensiometer for all spinning conditions are listed in the above Table II. Within the measuring range of the Tensiometer, there is no different take-up force between spinning conditions that can be detected, because both the air drag force F_{aero} [estimated using eqs. (6), (8), and (9)] and inertial force F_{inert} [calculated using eq. (7)] at a distance 180 cm from the spinneret are too small in comparison with the total force and they do not have any effect on the total force. It is seen from Figure 10(b) that total forces of the air drag plus inertial force at a distance 180 cm below the die exit for different spinning conditions have minimum and maximum values of 0.00071 cN and 0.0071 cN, respectively. This result shows a considerable difference in force value between different spinning conditions, but this force value is too small in comparison with the take-up

force $F_L = 1.9$ cN, determined using a tensiometer. Therefore, it is simplify assumed that the take-up force F_L is constant for all spinning conditions. For the calculations of tensile force $F(x)$ [after eqs. (17) and (18)], tensile stress $\sigma(x)$ [after eq. (19)], and apparent elongational viscosity $\eta_{app}(x)$ [after eq. (20)], the measured and interpolated values of $v(x)$ were always used.

Figures 11 and 12 show the distributions of the tensile force along the spinline for different spinning conditions. It can be seen that the tensile force is nearly constant along the spinline [Figures 11(a) and 12(a)]. The tensile force slightly increases with increasing the mass flow rate at the constant take-up velocity of 50 m min^{-1} [Figure 11(b)] or with decreasing the take-up velocity at the constant mass flow rate of 1.0 g min^{-1} [Figure 12(b)]. This tendency is due to the differences of filament diameter (Figure 9), which affect the gravitational force.

For each spinning condition, the filament diameter decreased along the spinline in the fiber formation zone (Figure 9). This decrease leads to the considerable increase of the tensile stress (Figure 13), although the variation of tensile force along the spinline is very small [Figures 11(a) and 12(a)].

Figure 14 shows the calculated apparent elongational viscosity (APEV) of PLA/PVA filaments versus distance from spinneret for different spinning conditions. It is seen that the APEV keeps an almost constant value at the first 10 cm. It then rapidly increases and goes to infinity, where the attenuation process is finished [Figure 14(a,b)]. It is seen from Figure 14(a) that as the mass flow rate increases the APEV reaches an infinite value more slowly, because the filament cools more slowly along the spinline (Figure 4). Figure 14(b) shows an interesting relationship between the APEV and the take-up velocity. In general, as the take-up velocities decreases, the APEV becomes infinite at the shorter distances from the spinneret. However, this tendency is not found at a take-up velocity of 70 m min^{-1}. The APEV at this take up velocity goes to infinity even earlier than that of take-up velocities of 30 and 50 m min^{-1}. An explanation of this behavior is that the melt spinning process with take-up velocity of 70 m min^{-1} is faster terminated than that of with take-up velocity of 30 and 50 m min^{-1}. This agrees well with the velocity results that have already shown in Figure 8(a).

As mentioned above, the APEV depends on the ASR after eq. (20). It depends also on filament temperature: as the filament temperature decreases, the APEV increases. The temperature profiles in Figure 5 show that there are no significant differences of the filament temperature between various take-up velocities, that why they can be fitted from the same eq. (15). However, the experimental results of filament temperature in Appendix show a little difference. The filament in the melt spinning process with the take-up velocity of 70 m min^{-1} is quenched a little earlier than that with take-up velocities of 30 and 50 m min^{-1}.

It is worth pointing out from Figure 14(c,d) that the APEV has a minimum value at several centimeters below the spinneret, where the maximum ASR values are found [Figures 7(b) and 8(b)]. This phenomenon is an expression that the APEV is
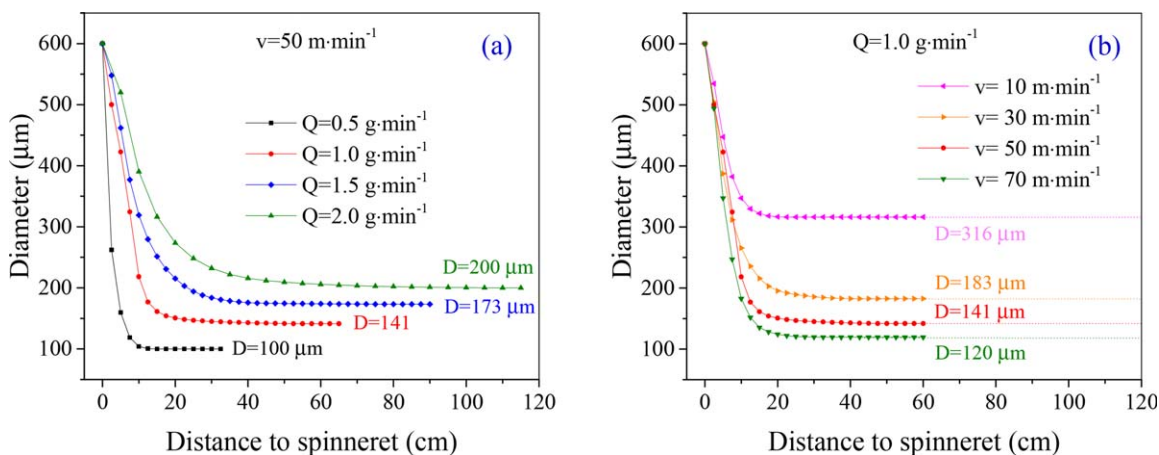
Figure 9. Filament diameter versus distance for the different spinning conditions: (a) different mass flow rates and constant take-up velocity, (b) different take-up velocities and constant mass flow rate. [Color figure can be viewed in the online issue, which is available at wileyonlinelibrary.com.]

inversely proportional to the ASR after eq. (20), which also can be written as $\eta_{app} = \frac{F \cdot v}{V \cdot v'}$.

DISCUSSION OF THE LENGTH OF THE FIBER FORMATION ZONE

In the melt spinning process, the fiber formation zone is defined as the distance L_S from the die exit x_0 $(x = 0)$ to the solidification point x_s $(x = s)$, where the fiber becomes solid. In this zone, the morphological development of the filament occurs and it is affected by the courses of spinning parameters as analyzed above. Below solidification point no further deformation of the filament occurs, i.e., the process of morphological development of filaments no more happens.

In principle, at the same time, the filament velocity should reach the take-up velocity and filament temperature should cool down to its glass transition temperature T_g at the same solidification distance L_S. Figure 15 plots the solidification distance versus mass flow rate and take-up velocity from the fitted velocity (Filament Velocity and Velocity Gradient along the Spinline section) and fitted temperature profiles (Filament Temperature

Profiles section). For all analyses below, it is assumed that T_g of the PLA/PVA filaments from fitted temperature profiles is equal to $T_{g,DSC}$ of PLA/PVA blends obtained by DSC measurements. The difference between T_g and $T_{g,DSC}$ can be explained with the different thermal behavior of polymers in DSC measurements and in the melt spinning process due to the different equilibrium and non-equilibrium states.[12] It is seen from Figure 15 that the distance L_{Sv} in which the filament velocity reaches its take-up velocity, i.e., the solidification distance obtained from velocity profiles, is always shorter than the solidification distance L_{ST} obtained from the fitted temperature profiles $(L_{Sv} < L_{ST})$. This interesting phenomenon may occur for the low melt spinning speed up to 70 m min^{-1}. It may be that filament needs more time to go to its glass transition temperature than to reaches its take-up velocity or very near take-up velocity.

The following eqs. (21) and (22) were used to calculate the time t_{Sv} required for the filament velocity reaches its take-up velocity and the time t_{ST} needed for the filament temperature goes to its glass transition temperature, respectively.
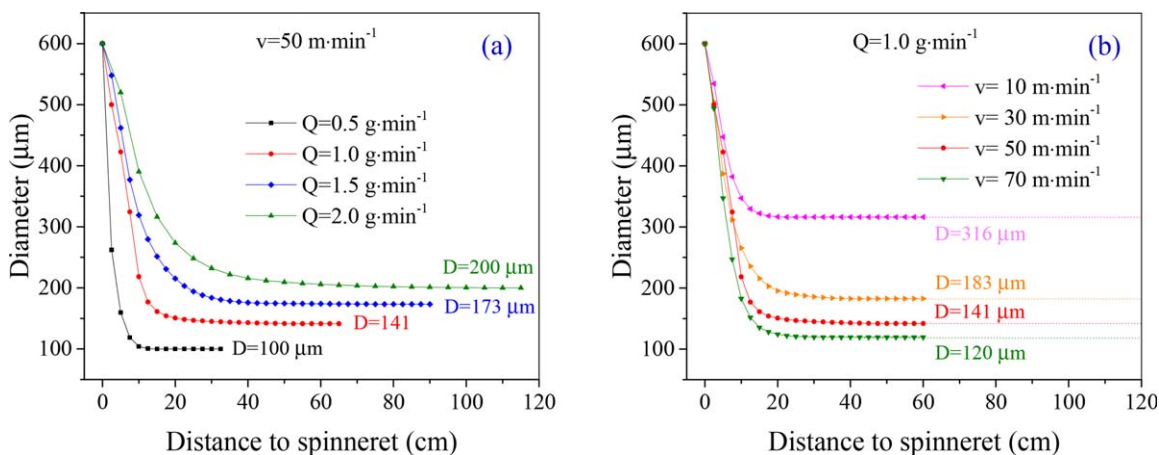

Figure 10. Calculated air drag and inertial force at a distance 180 cm from the spinneret for different spinning conditions: (a) different mass flow rates and constant take-up velocity, (b) different take-up velocities and constant mass flow rate. [Color figure can be viewed in the online issue, which is available at wileyonlinelibrary.com.]
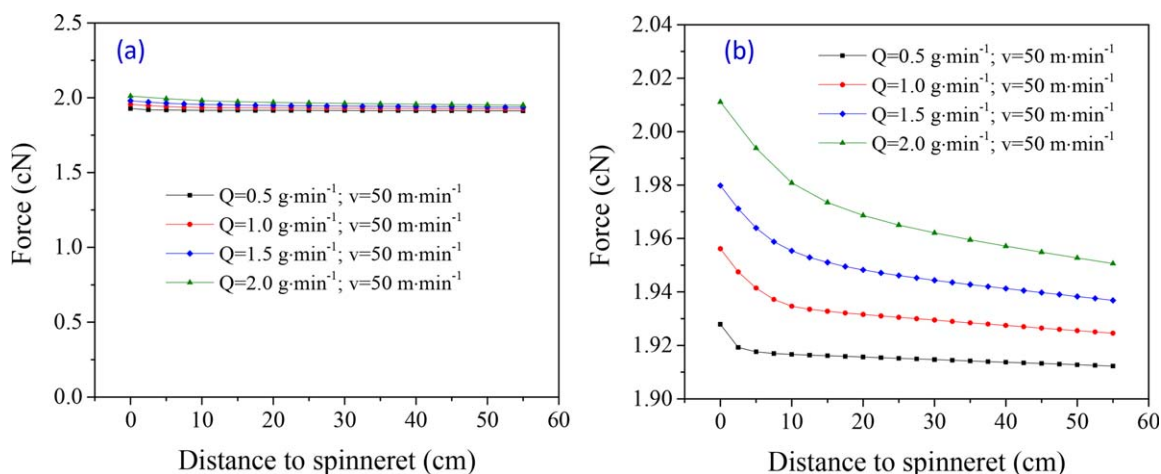
Figure 11. Tensile force versus distance for the spinning condition A: vertical *y*-axis from 0.0 to 2.5 (a), and 1.90 to 2.04 (b). [Color figure can be viewed in the online issue, which is available at wileyonlinelibrary.com.]

$$t_{Sv} = \int_{x_0}^{x_{Sv}} \frac{1}{v(x)} \, dx \qquad (21)$$

$$t_{ST} = \int_{x_0}^{x_{ST}} \frac{1}{v(x)} \, dx \qquad (22)$$

where, x_{Sv} and x_{ST} are the solidification points from the fitted velocity profiles and the fitted temperature profiles.

The time difference $\Delta t = t_{ST} - t_{Sv}$ changes a little over a range of 0.12 to 0.21 s for the constant take-up velocity and different mass flow rates [Figure 16(a)]. It is also seen from Figure 16(b) that there is no substantial time difference Δt for the take-up velocity of 30, 50, and 70 m min^{-1}, but except for the very slow take-up velocity of 10 m min^{-1}. The final filament diameter of the take-up velocity of 10 m min^{-1} is 318 μm almost twice as large as that of the take-up velocity of 30 m min^{-1}. This means that the filament at the take-up velocity of 10 m min^{-1} need much more time that at the higher take-up velocities for cooling down to its glass transition temperature although the filament velocity has already reached its take-up velocity.

The difference between the solidification distances L_{Sv} and L_{ST} can be explained as follows: (1) The axial heat conduction effect of the filament along the spinline and the nonuniform radial temperature through the cross-section of the thick filament, leads to a cooler outer layer of the filament in comparison with the inner layer. (2) The occurrence of a telescoping effect or "necking" during stretching the filament within fiber formation zone. (3) The two measurement methods (LDV and infrared thermography) are differences themselves.

In summary, considering the length of fiber deformation zone, it is reasonable to assume that the fiber formation zone is from the die exit to the point at the filament velocity reaches its take-up velocity. The end of deformation point equals the first point along the spinline where filament velocity reaches its take-up velocity or very near take-up velocity. In this zone, the morphological development of PLA/PVA blends is mainly deformed by the increase of velocity and tensile stress.
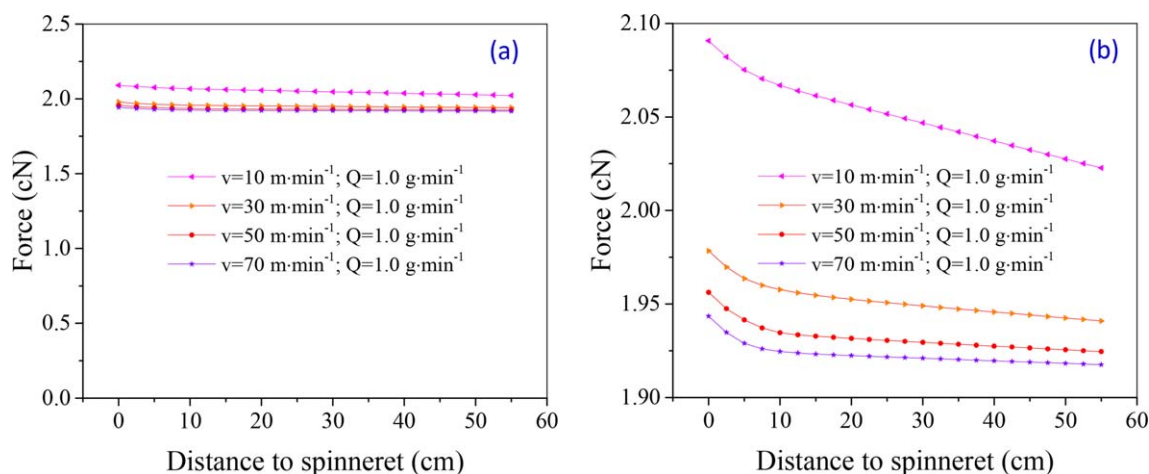

Figure 12. Tensile force versus distance for the spinning condition B: vertical *y*-axis from 0.0 to 2.5 (a), and 1.90 to 2.10 (b). [Color figure can be viewed in the online issue, which is available at wileyonlinelibrary.com.]
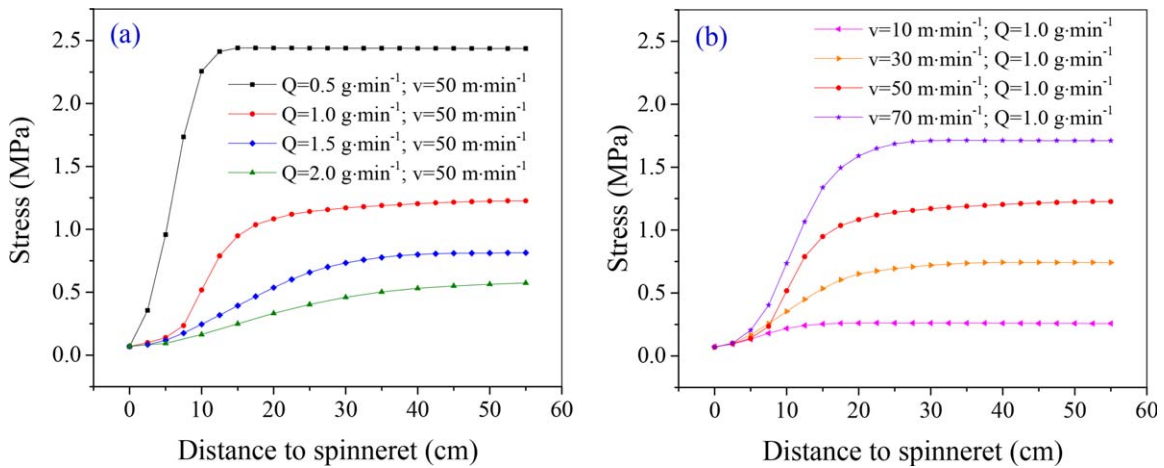
Figure 13. Tensile stress versus distance for the spinning condition A (a) and B (b). [Color figure can be viewed in the online issue, which is available at wileyonlinelibrary.com.]
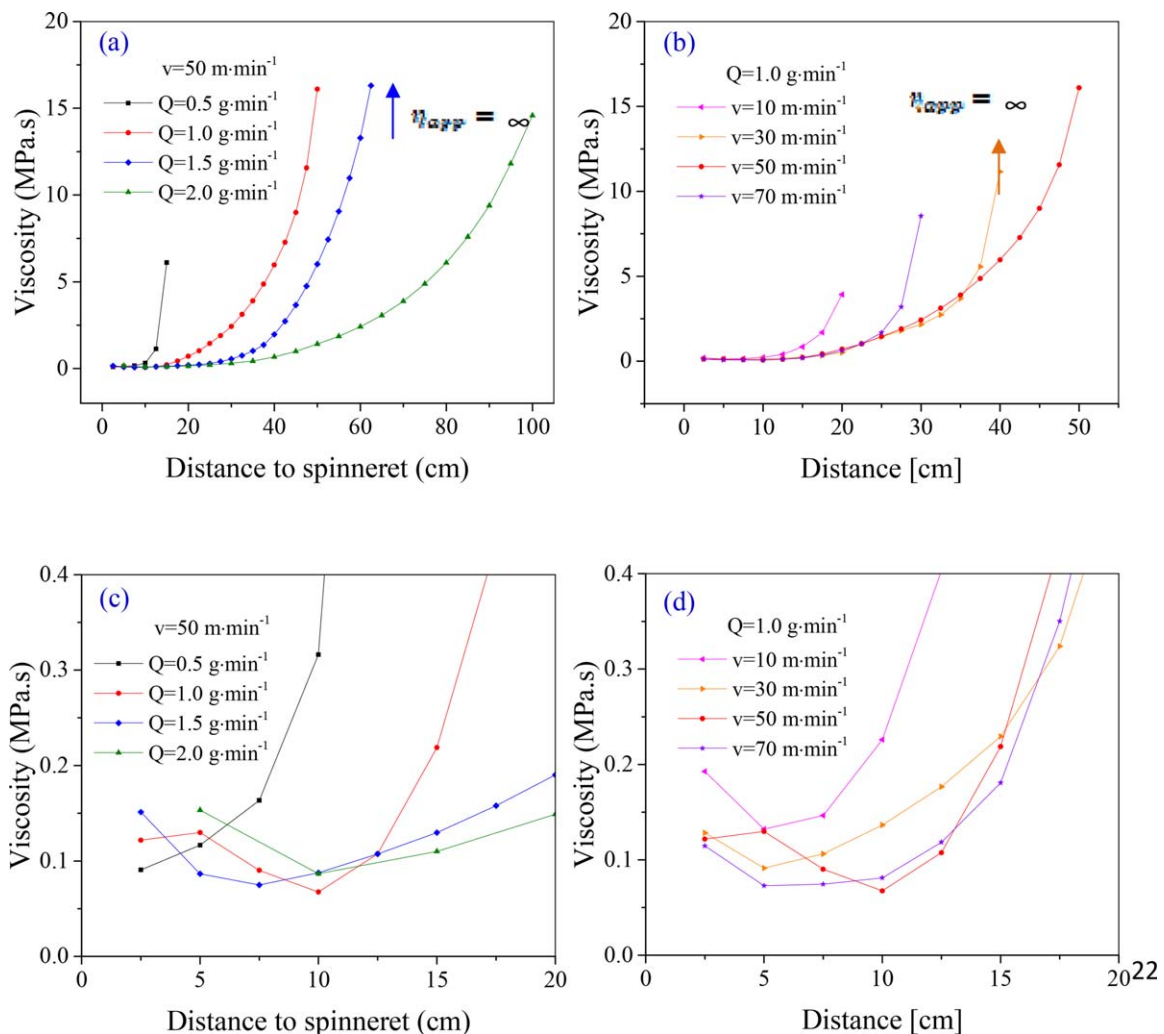

Figure 14. Apparent elongational viscosity versus distance for the spinning condition A (a,c) and spinning condition B (b,d). [Color figure can be viewed in the online issue, which is available at wileyonlinelibrary.com.]
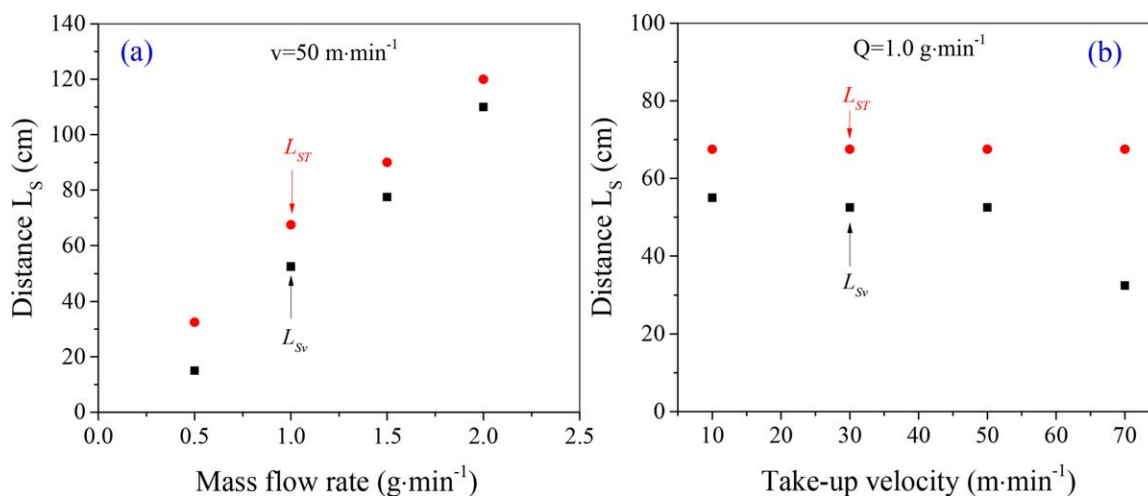
Figure 15. Solidification distance from fitted temperature profiles L_{ST} [the red-colored filled circle (●)] and fitted velocity profiles L_{Sv} [the black-colored filled square (■)] versus mass flow rate (a) and versus take-up velocity (b). [Color figure can be viewed in the online issue, which is available at wileyonlinelibrary.com.]
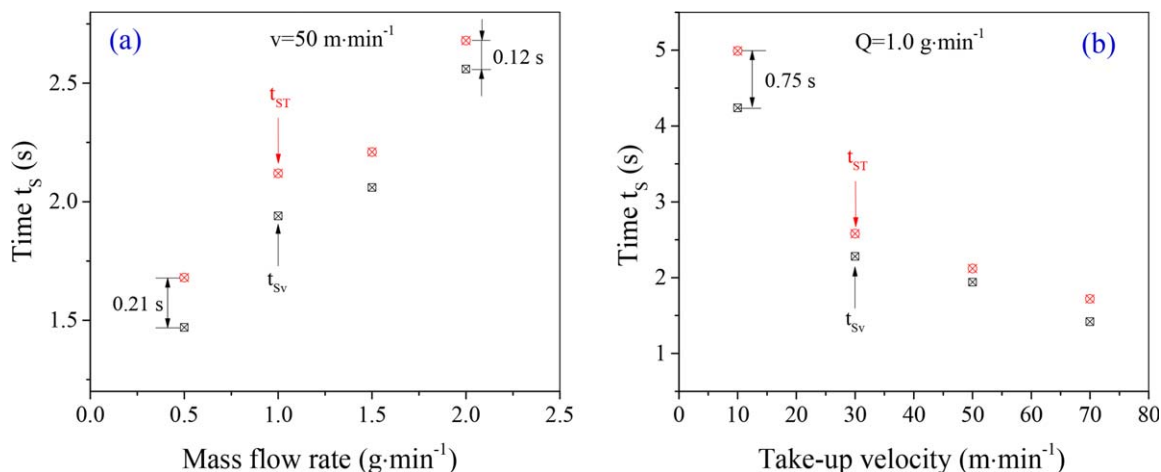

Figure 16. Solidification time versus mass flow rate (a) and take-up velocity (b). [Color figure can be viewed in the online issue, which is available at wileyonlinelibrary.com.]

CONCLUSIONS

The profiles of PLA/PVA filament parameters such as temperature, velocity, axial strain rate, diameter, tensile stress, etc. along the spinline in the low-speed melt spinning process with take-up velocity up to 70 m min^{-1} were investigated. It was found that the melt spinning of extremely high viscosity materials such PLA/PVA blends at very low take-up velocities is very different from standard spinning velocities of 1000 to 4000 m min^{-1} and high spinning velocities over 4000 m min^{-1}.

Regarding the length of the fiber formation zone, it was found that there is the difference between solidification lengths determined from velocity profiles L_{Sv} and from temperature profiles L_{ST} ($L_{Sv} < L_{ST}$). This unexpected phenomenon may happen for the low-speed melt spinning process due to the axial heat conduction effect of the filament along the spinline and the radial temperature distribution through the cross-sectional thick filament. By considering the length of fiber deformation zone, it is

assume that the fiber formation zone is from the die exit to the point at the filament velocity reaches its take-up velocity. In this zone, the morphological development of PLA/PVA blends is mainly deformed by the increase of velocity and tensile stress.

Concerning the heat transfer from filament surface into the surrounding air, it was found that the Nusselt number is nearly constant along the spinline and has values 0.85 and 0.90 (see in Appendix). By using these constant Nusselt numbers, the mathematical simulation of the filament temperature profiles along spinline in the low-speed melt spinning process becomes much simpler. The simulated results agree very well with the measured values of filament temperatures and even they agree with the filament temperature profiles calculated using the often used Kase and Matsuo model.

Another remarkable finding of the present study is related to air drag and the inertial force values which are small in comparison with the total force, and they do not have any effect on the total

force in the low-speed melt spinning process. The tensile forces are nearly constant along the spinline.

ACKNOWLEDGMENTS

APPENDIX

Figures A.1 and Appendix A2 show the experimental results and their comparison with our simulated results as well as with Kase and Matsuo model. The gray cross symbols (×) present for the filament temperature values obtained using an Infrared camera as mentioned in Online Filament Temperature Measurements section. Points (including deviation) are the corrected temperatures by emissivity. The dash curves (− − −) are the temperature curves, fitted by using different exponential decay functions as follow:

Appendix A.I. Various Constant Value u for Different Spinning Conditions used for the General Exponential Decay Function $a1$

| Conditions	Take-up velocity (m min^{-1})	Mass flow rate (g min^{-1})	constant value u (-)
A	50	0.5	21
		1.0	42
		1.5	57
		2.0	75
B	10		42
	30	1.0	42
	50		42
	70		42

For the constant mass flow rate, the constant value u is independent of take-up velocity and it has a value of 42.

$$T(x) = T_{air} + (T_0 - T_{air}) \times \exp\left(-\frac{x}{u}\right) \qquad (A.1)$$

where $T_{air} = 25\,°C$ and $T_0 = 195\,°C$ are the temperature of the ambient air and the temperature of molten filament at die exit ($x = 0$), respectively, x is the distance from the spinneret, and
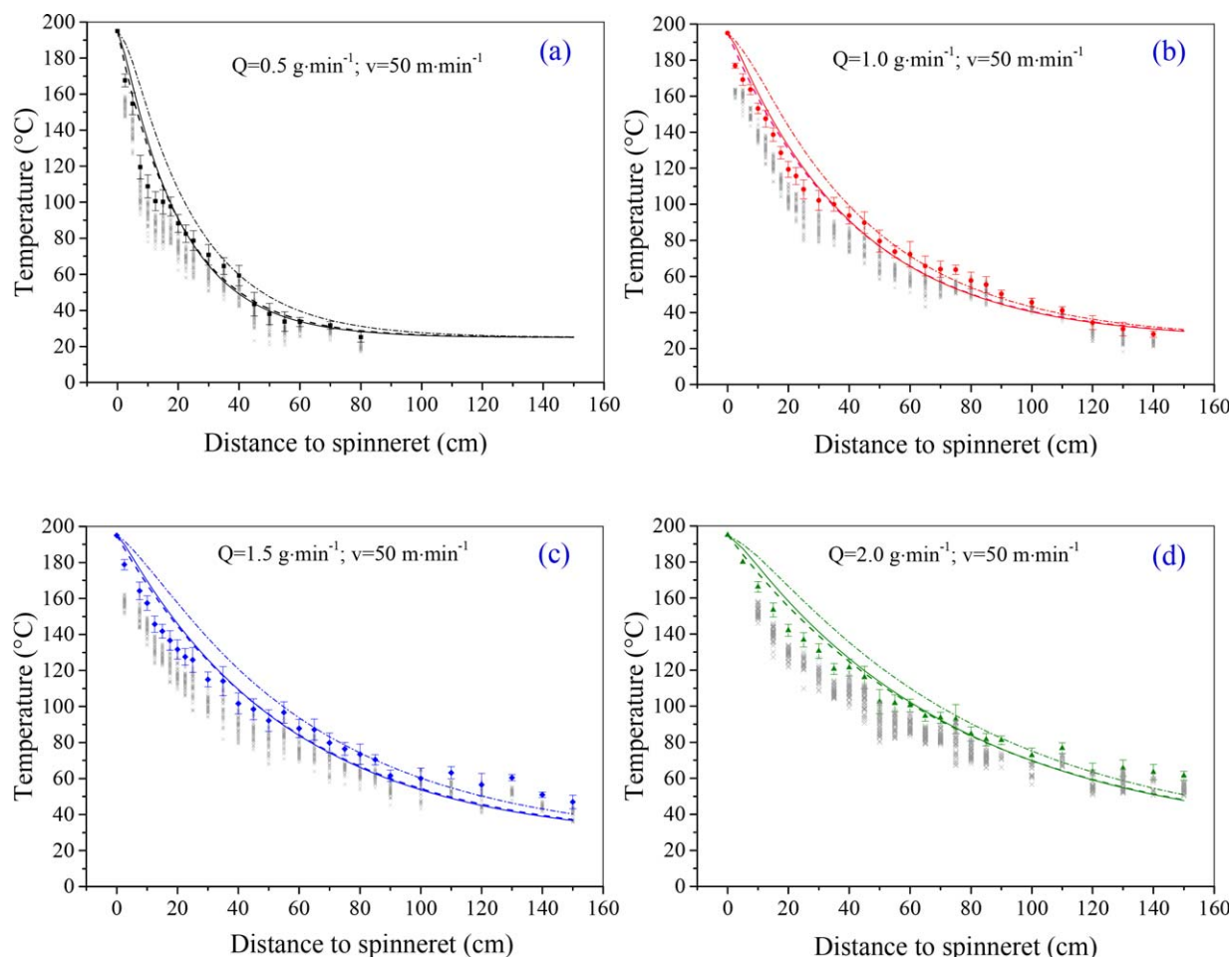
Appendix A1. Filament temperature versus distance for the different mass flow rate of 0.5 g min^{-1} (a), 1.0 g min^{-1} (b), 1.5 g min^{-1} (c), and 2.0 g min^{-1} (d) at the take-up velocity of 50 m min^{-1}. [Color figure can be viewed in the online issue, which is available at wileyonlinelibrary.com.]
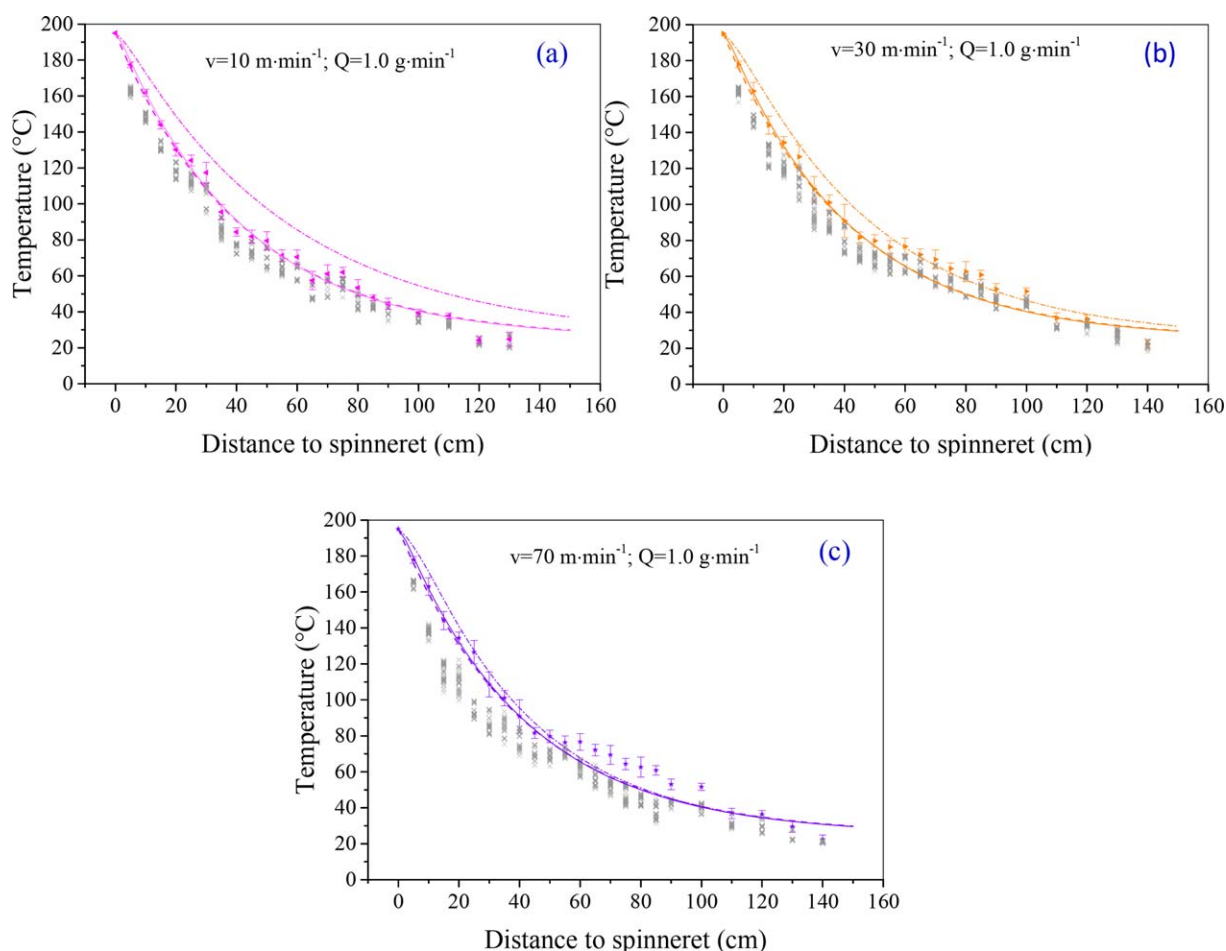
Appendix A2. Filament temperature versus distance for the mass flow rate of 1.0 g min^{-1} at the different take-up velocity of 10 m min^{-1} (a), 30 m min^{-1} (b), and 70 m min^{-1} (c). [Color figure can be viewed in the online issue, which is available at wileyonlinelibrary.com.]

different constant u values for different spinning conditions are listed in Table A1. The continuous curves ( ) are the simulated curves, and the dash dot curves ( ) present the filament temperature profiles obtained using the Kase and Matsuo model. It can be seen that the simulated results agreed well with measured values of fitted temperature. The simulated PLA/PVA filament temperature slightly cooled faster than the PLA/PVA filament temperature obtained using the Kase and Matsuo.

The simulated temperature profiles (the continuous curves) and the temperature profiles using the Kase and Matsuo model (the dash dot curves) were determined using the following eq. (A.2), which is simplified from eq. (10) with an assumption that the PLA/PVA filament may not crystallize during melt spinning in the low take-up speed spinning process.

$$\frac{dT(x)}{dx} = -(T(x) - T_{\text{air}}(x)).N_u \frac{\pi.\lambda_{\text{air}}}{Q.c_P} \qquad (A.2)$$

where, the temperature of surrouding air T_{air} is 25 °C, the heat conductivity of air at 25 °C λ_{air} is 0.026 W m^{-1} K^{-1}, and the heat capacity of PLA/PVA blend c_P is 1.80 J g^{-1} K^{-1}, was obtained using DSC measurement. The Nusselt number N_u after the Kase and Mutsuo model is followed by eq. (11). In this study, the Nusselt number N_u for the simulation was estimated by
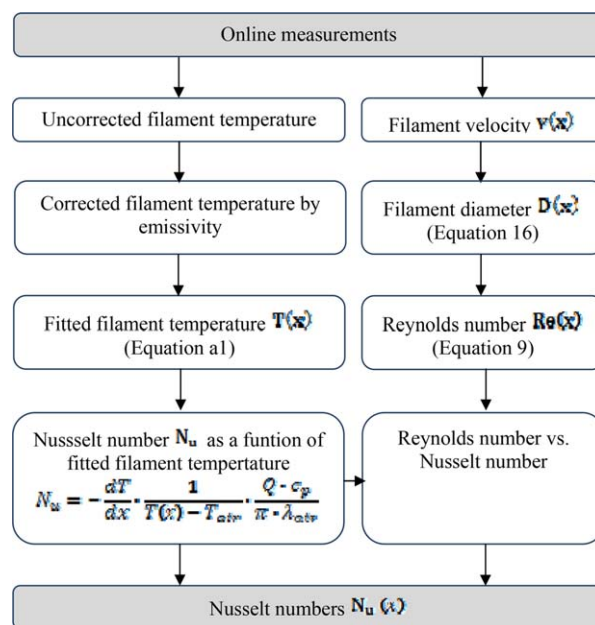
Appendix A3. Flow diagram for estimation of Nusselt number from experimental results of filament temperature and velocity. [Color figure can be viewed in the online issue, which is available at wileyonlinelibrary.com.]
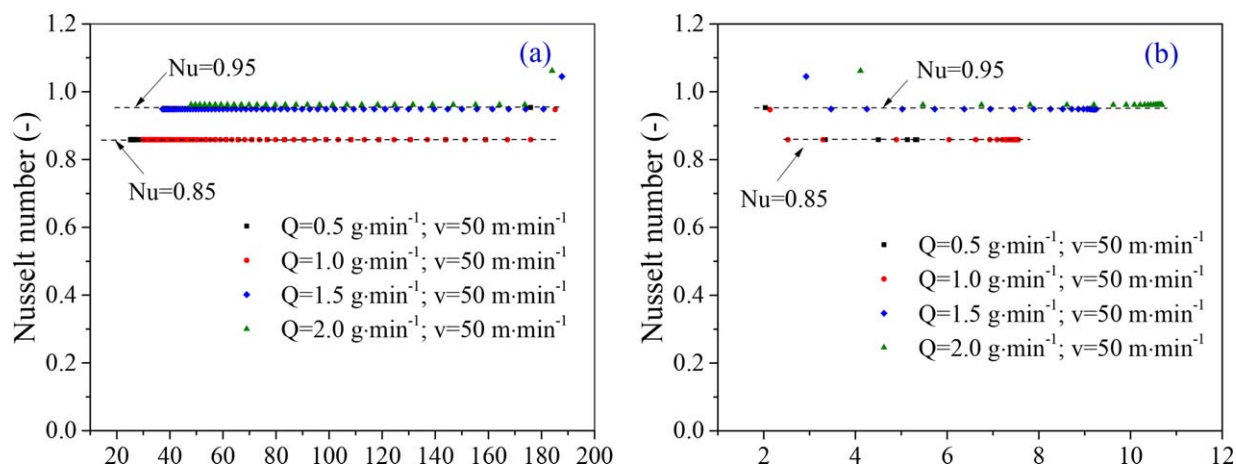
Appendix A.4. Nusselt number versus temperature (a) and Nusselt number versus Reynolds number (b) for the different mass flow rates at the take-up velocity of 50 m min^{-1}. [Color figure can be viewed in the online issue, which is available at wileyonlinelibrary.com.]

considering the relationship between the Nusselt number versus Filament temperature as well as The Nusselt number versus Reynolds number, which is schematically presented in Figure Appendix A3.

It is seen from Figure Appendix A.4 that the Nusselt number is nearly constant along the spinline. The Nusselt number has higher values at the higher amount of mass flow rates. However, there is little difference between the Nusselt number of the mass flow rates of 0.5, 1.0 g min^{-1} and that of the mass flow rates of 1.5, 2.0 g min^{-1} at the constant take-up velocity of 50 m min^{-1}. For the constant mass flow rate of 1.0 g min^{-1}, the Nusselt number is also nearly constant and has the same value of 0.85 at the different velocities up to 70 m min^{-1} due to the same the fitted temperature profiles. In this study, the Nusselt number is approximately considered as a constant value of 0.85 if $Q \leq 1.0$ g min^{-1} and 0.95 if $1.0 < Q \leq 2.0$ g min^{-1} independent of take-up velocities within the above range of Reynolds number.

REFERENCES

1. Miller, W. A.; Merriam, J. C. N. U.S. Pat. 3,097,991 (**1963**).
2. Wang, D.; Sun, G. *Eur. Polym. J.* **2007**, *43*, 3587.
3. Bhattacharyya, D.; Fakirov, S. In Nano- and Micromechanics of Polymer Blends and Composites; Karger-Kocsis, J.; Fakirov, S., Eds.; Carl Hanser Verlag: Munich, **2009**; Chapter 5, p 167.
4. Fakirov, S. In Synthetic Polymer-Polymer Composites; Bhattacharyya, D.; Fakirov, S., Eds.; Carl Hanser Verlag GmbH: Munich, **2012**; Chapter 11, p 353.
5. Lin, S. T. C.; Bhattacharyya, D.; Fakirov, S.; Cornish, J. *Int. J. Polym. Mater.* **2014**, *63*, 416.
6. Tran, N. H. A.; Brünig, H.; Hinüber, C.; Heinrich, G. *Macromol. Mater. Eng.* **2014**, *299*, 219.
7. Tran, N. H. A.; Brünig, H.; Boldt, R.; Heinrich, G. *Polymer* **2014**, *55*, 6354.
8. Denn, M. M. In Computational Analysis of Polymer Processing; Pearson, J. R. A.; Richardson, S. M., Eds.; Springer: Netherlands, **1983**; Chapter 7, p 179.
9. Ziabicki, A. Fundamentals of Fibre Formation: The Science of Fibre Spinning and Drawing; Wiley: New York, **1976**.
10. Ziabicki, A.; Kawai, H. High-Speed Fiber Spinning: Science and Engineering Aspects; Wiley: New York, **1985**.
11. Takajima, T.; Kajiwara, K.; McIntyre, J. E. Advanced Fiber Spinning Technology; Woodhead Publishing Company: Cambridge, **1994**.
12. Beyreuther, R.; Brünig, H. Dynamics of Fibre Formation and Processing: Modelling and Application in Fibre and Textile Industry; Springer: Berlin Heidelberg, **2007**.
13. Ziabicki, A. *Kolloid-Zeitschrift* **1961**, *175*, 14.
14. Hamana, I. *Lenzinger Berichte* **1968**, *26*, 118.
15. Kase, S.; Matsuo, T. *J. Polym. Sci. Part A* **1965**, *3*, 2541.
16. Golzar, M.; Beyreuther, R.; Brünig, H.; Tändler, B.; Vogel, R. *Adv. Polym. Technol.* **2004**, *23*, 176.
17. Vogel, R.; Hatzikiriakos, S. G.; Brünig, H.; Tändler, B.; Golzar, M. *Int. Polym. Proc.* **2003**, *18*, 67.
18. Oh, T. *Polym. Eng. Sci.* **2006**, *46*, 609.
19. Kase, S.; Matsuo, T. *J. Appl. Polym. Sci.* **1967**, *11*, 251.
20. Matovich, M. A.; Pearson, J. R. A. *Ind. Eng. Chem. Fundam.* **1969**, *8*, 512.
21. Shah, Y. T.; Pearson, J. R. A. *Ind. Eng. Chem. Fundam.* **1972**, *11*, 145.